The following publication Z. Liu, D. Xie, L. Wang, J. Fang, Z. Wei and C. Yu, "RIS-Mounted UAV Millimeter-Wave Communications Across Diverse Scenarios: Path-Loss Model, Beam Management, and Posture Analysis," in IEEE Transactions on Communications, vol. 74, pp. 1717-1731, 2026 is available at https://doi.org/10.1109/TCOMM.2025.3637073.

RIS-mounted UAV Millimeter-wave Communications Across Diverse Scenarios: Path-loss Model, Beam Management and Posture Analysis

Zhongxu Liu, Dawei Xie, Luyao Wang, Junbin Fang, *Member, IEEE,* Zixian Wei, *Member, IEEE,* and Changyuan Yu, *Senior Member, IEEE*

***Abstract*—Oriented to low-altitude economy, integrated air-ground-space communication system and ultra-dense mobile communication network access, reconfigurable intelligent surfaces-mounted unmanned aerial vehicle (RIS-UAV) offer a dynamic solution for propagation challenges in millimeter-wave (mmWave) communications. This work aims to present a comprehensive analytical framework for RIS-UAV assisted mmWave communications in multiple scenarios, encompassing single-base station single-user terminal (SBSU), single-base station multi-user terminal (SBMU), multi-base station single-user terminal (MBSU), and multi-base station multi-user terminal (MBMU) scenarios. We first establish path-loss models and flexible beam management considering UAV translational and rotational posture movements separately within the SBSU scenario. For multi-user scenarios, we propose a space division multiple access (SDMA) over RIS scheme leveraging RIS element partitioning. For multi-base station scenarios, a mobile RIS-UAV phase coordination (MRUPC) strategy is proposed, utilizing the controlled mobility of the UAV to simplify phase compensation requirements for signals from multiple base stations. Extensive numerical simulations validate the accuracy of the derived path-loss model and the feasibility of the proposed beam management scheme for each scenario. The results demonstrate that SDMA over RIS effectively achieves multi-user mmWave beamforming. In addition, the proposed MRUPC strategy exhibits substantial performance gains (approx. 6-8 dB) over the static scheme in the MBSU scenario, validating the feasibility and superiority of leveraging UAV mobility for multi-base station coordination. This study comprehensively provides a systematic theoretical foundation and physical-layer solutions for the design and flexible deployment of joint RIS-UAV mmWave systems in complex wireless access scenarios.**

***Index Terms*—Unmanned aerial vehicles, Millimeter-wave communications, Reconfigurable intelligent surfaces, Path-loss model, Beam forming and management.**

I. INTRODUCTION

THE rapid growth of emerging access applications, such as virtual reality, augmented reality, and high definition video streaming, imposes increasing demands on higher data transmission rates and denser access networking in wireless communication systems [1, 2]. To satisfy these requirements, the exploration and deployment of advanced wireless communication technologies have become imperative. As an important link in the development of low-altitude economy and beyond fifth/sixth-generation (B5G/6G) mobile networks, millimeter wave (mmWave) communication leveraging the vast untapped spectrum resources within the 30-300 GHz range, offers crucial potential for realizing ultra-high data rates [3–5]. However, despite its potential for greatly improved spectral efficiency, mmWave signal propagation suffers from inherent physical challenges: high-frequency signals not only experience severe path loss, proportional to the square of the frequency during free-space propagation [6], but also exhibit extremely limited penetration capabilities through obstacles and poor diffraction properties [7]. These physical-layer limitations constitute a critical bottleneck for conventional mmWave systems in providing reliable, wide-area coverage within dynamic and complex environments, significantly hindering their widespread adoption in B5G/6G.

Against this backdrop, reconfigurable intelligent surfaces (RIS) have recently emerged as a transformative solution. Comprised of many passive reflecting elements, a RIS can dynamically adjust each element's amplitude and phase to precisely steer incident electromagnetic waves [8, 9]. A growing body of work has demonstrated that RIS can effectively mitigate the propagation deficiencies of mmWave signals, significantly enhancing their coverage range and communication reliability. For example, Ref. [10] substantiated the efficacy of RIS as an effective reflector in vehicular communication scenarios where the line-of-sight (LoS) path is obstructed. Ref. [11] , employing stochastic geometry theory, formulated an analytical framework for RIS-assisted mmWave networks, quantitatively verifying its positive impact on network coverage performance. Furthermore, Ref. [12] applied a Neyman–Pearson criterion to design blockage aware algorithms and robust beamforming, thereby strengthening interference resilience.

Although static RIS deployments have yielded promising results, they struggle to maintain optimal reflection paths in scenarios involving user mobility. To overcome this, researchers have proposed mounting RIS on the unmanned aerial vehicle (UAV), leveraging UAV's three-dimensional mobility to establish high-quality flexible links between base stations and users under blocked LoS conditions [13, 14]. This RIS-mounted UAV (RIS-UAV) paradigm breaks free from the physical limitations of static RIS and introduces a new approach for extending mmWave deployment and coverage.

This work is supported by HK RGC GRF15209321, and HK RGC Junior Research Fellow Scheme under Grants JRFS2526-5S09. (Corresponding author: Zixian Wei and Changyuan Yu)

Zhongxu Liu, Dawei Xie, Zixian Wei, and Changyuan Yu are with Photonics Research Institute, Department of Electrical and Electronic Engineering, The Hong Kong Polytechnic University, Hong Kong 999077, China (e-mail: zhongxu,liu@connect.polyu.hk, dawei.xie@connect.polyu.hk, zixian.wei@polyu.edu.hk, changyuan.yu@polyu.edu.hk)

L. Wang is with the Department of Internet of Things Engineering, Jinan University, Zhuhai 519070, China. (e-mail: wangluyao231@mails.ucas.ac.cn)

J. Fang is with the Guangdong Provincial Key Laboratory of Optical Fiber Sensing and Communications, Guangdong Provincial Engineering Technology Research Center on Visible Light Communication, Guangzhou Municipal Key Laboratory of Engineering Technology on Visible Light Communication and Department of Optoelectronic Engineering, Jinan University, Guangzhou 510632, China. (e-mail: tjunbinfang@jnu.edu.cn).

Within this emerging field, current studies concentrate on three primary objectives: (i) Enhancing signal coverage and transmission range, with particular emphasis on extending service areas in challenging propagation environments or providing supplementary coverage for specific high-demand hotspots, as exemplified by [15] which optimizes RIS-UAV deployment for hotspot servicing, and [16] which employs a dual-RIS panel design to assist cellular user offloading, indirectly addressing inter-cell coverage and load balancing; (ii) Improving data rates and system throughput, where extensive efforts have been dedicated to designing joint optimization schemes, involving UAV trajectory, RIS phase shifts, power allocation, etc. to maximize channel capacity, user rates, or overall system throughput [17–21], with some studies additionally considering multi-user fairness [22] or UAV energy consumption constraints [23]; (iii) Enhancing communication security, for instance, by utilizing specially designed multi-functional RIS to simultaneously reflect desired signals and generate jamming signals against eavesdroppers [24], or by employing machine learning to maximize system secrecy rates while guaranteeing legitimate users' quality of service requirements [25, 26].

However, existing studies exhibit several limitations. Firstly, while UAV trajectory optimization is well studied, the effects of UAV postures, particularly translational and rotational movements, on beam management and path loss have received little attention. On the one hand, the UAV will experience rapid position movement and attitude changes (yaw, pitch, roll) during flight, which will cause high Doppler shift, fast fading, beam misalignment, and link outage. On the other hand, during the suspension process, the UAV will be affected by wind, air pressure, mechanical vibration, etc., which will cause physical disturbances on the RIS panel and further cause phase control errors. Secondly, existing multi-user access schemes often rely on time division multiplexing [22] or frequency division multiplexing [27], which suffer from low spectral efficiency, or on non-orthogonal multiple access (NOMA) [23, 28], which increases receiver complexity and error propagation due to successive interference cancellation. Moreover, most work focuses on single base station scenarios, including single-base station single-user terminal (SBSU) [24–26] and single-base station multi-user terminal (SBMU) [27–29], with scant exploration of multi-base station single-user terminal (MBSU) and multi-base station multi-user terminal (MBMU) settings. Although [16] considers two base stations, it sidesteps the challenge of coordinating multiple sources by using a dual-panel RIS. Furthermore, prior research has yet to fully leverage UAV mobility itself to resolve phase compensation conflicts in multi-base station deployments.

To address these challenges and extend RIS-UAV to broader scenarios while accounting for UAV dynamics and multi-user access, this paper presents a comprehensive investigation. We begin by modeling and analyzing the specific impacts of translational or rotational UAV movements on the path loss model and RIS phase-shift design. Building upon this foundation, we systematically extend the path-loss model and beam management to SBMU, MBSU, and MBMU configurations. For multi-user environments, we introduce a spatial division multiplexing (SDMA) over RIS scheme for user access and management. Crucially, for multi-base station scenarios, we propose a mobile RIS-UAV phase coordination (MRUPC) strategy that uses controlled UAV mobility to adjust positioning proactively, thereby simplifying the phase compensation requirements for a single RIS coordinating signals from multiple base stations.

The main contributions of this paper are summarized as follows:

(i) First, we establish a systematic and unified analytical framework for RIS-UAV-assisted mmWave communication systems. This framework is the first of its kind to enable a coherent analysis and fair comparison across four fundamental scenarios of escalating complexity. We start by developing a foundational path-loss model and beam management for the elemental SBSU case with a dedicated study of UAV translation and rotation effects. Then, systematically based on this foundation, we introduce tailored beam management and coordination strategies to address the unique challenges of multi-user and multi-station environments.

(ii) Second, for multi-user scenarios, we introduce a novel SDMA over RIS scheme. This approach partitions RIS elements to serve different users concurrently within the same time-frequency resources. It boosts resource utilization while strategically avoiding the high complexity and error propagation risk inherent in NOMA's SIC receivers.

(iii) Third, for multi-cell scenarios, we propose an innovative MURPC strategy. This strategy uniquely leverages controlled UAV positioning as a solution to alleviate stringent phase-compensation requirements for a single RIS. It offers a flexible and potentially more cost-effective alternative to hardware-intensive multi-panel RIS solutions, transforming a mobility challenge into a system design advantage.

The rest of the paper is organized as follows. Chapter II first presents the path-loss model and beam management for RIS-UAV mmWave communication systems in the SBSU scenario, with separate analyses of the impacts of UAV translational and rotational movements. Subsequently, for the SBMU scenario, the phase design framework based on SDMA over RIS scheme is proposed. For MBSU and MBMU scenarios, the MRUPC scheme is adopted to design the phase shift of RIS. Chapter III conducts theoretical analysis and simulation validation of the RIS-UAV mmWave communication systems across SBSU, SBMU, MBSU, and MBMU scenarios, discussing computational results for system performance in each configuration. Chapter IV summarizes the key contributions and findings of this study.

II. PATH-LOSS MODEL AND BEAM MANAGEMENT

In this section, we address the diversity and complexity of RIS-UAV communication systems through a structured and progressive analytical framework. The general path-loss model for RIS-based mmWave communication systems serves as the common analytical basis across all configurations, ensuring a fair comparison. Building upon this unified foundation, we address the escalating complexity by introducing designed and novel beam management schemes for the specific challenges that emerge at each configuration. For multi-user interference

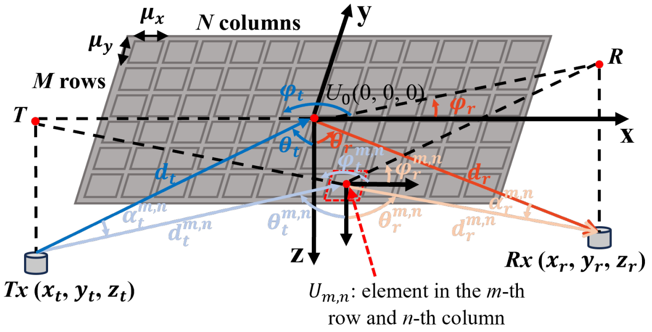

Fig. 1. Geometric model diagram of RIS-based NLoS links, where U_0 is the RIS center and $U_{m,n}$ is the (m, n)-th element.

in SBMU, we propose our SDMA over RIS scheme. For the multi-cell phase coordination challenge in MBSU, we introduce the innovative MURPC strategy. The most complex MBMU case is then handled by a synergistic integration of both strategies.

A. General Model of RIS-based mmWave Communication Links

Unlike traditional mmWave communication systems that rely on LoS links, the RIS-based mmWave communication system is predicated on non-line-of-sight (NLoS) links between the transmitter and receiver. Fig. 1 depicts the RIS-based NLoS link between the transmitting antenna T_x and receiving antenna R_x positioned at (x_t, y_t, z_t) and (x_r, y_r, z_r), respectively, with their X-Y plane projections marked as T and R. The RIS comprises an M × N element array on the X-Y plane, where all elements maintain a constant reflection amplitude A with independently controllable phase shifts $\omega_{m,n}$. With the RIS center U_0 located at the origin (0, 0, 0) and element dimensions u_x and u_y along the respective axes, the Cartesian coordinate of the (m, n)-th element $U_{m,n}$ is analytically expressed as $(u_x[(N + 1)/2–n], u_y[(M + 1)/2–m], 0)$. The dimensions of RIS elements are typically sub-wavelength, often in the order of λ/4 to λ/10, to allow for effective wavefront manipulation at the operational frequency. Other critical geometric parameters include: $d_t, d_t^{m,n}, d_r, d_r^{m,n}$ representing the Euclidean distance between T_x and U_0, between T_x and $U_{m,n}$, between U_0 and Rx and between $U_{m,n}$ and Rx, respectively; θ_t and $\theta_t^{m,n}$ denoting the elevation angles from U_0 and $U_{m,n}$ to Tx, with θ_r and $\theta_r^{m,n}$ corresponding to Rx; φ_t and $\varphi_t^{m,n}$ describing azimuth angles from U_0 and $U_{m,n}$ relative to Tx, while φ_r and $\varphi_r^{m,n}$ apply to Rx; additionally, $\alpha_t^{m,n}$ and $\alpha_r^{m,n}$ representing the elevation angle from Tx and Rx to $U_{m,n}$, respectively. Then, the received signal power at Rx reflected by RIS can be formulated as [30]:

$$P_r = P_t \frac{G_t G_r G \mu_x \mu_y \lambda^2}{64\pi^3} \times \left| \sum_{n=1}^{N} \sum_{m=1}^{M} \frac{\sqrt{\xi_{m,n}}}{d_t^{m,n} d_r^{m,n}} A e^{-j\left(\frac{2\pi(d_t^{m,n}+d_r^{m,n})}{\lambda} - \omega_{m,n}\right)} \right|^2. \tag{1}$$

In essence, this equation quantifies the received power as a product of the transmitted power (P_t), transmitting and receiving antenna gains (G_t and G_r), RIS unit gain ($G = 4\pi\mu_x\mu_y/\lambda^2$), and the squared magnitude of the coherent sum of signals from all RIS elements, where λ is the signal wavelength. Each element's contribution is weighted by the path loss of its individual link ($d_t^{m,n}$ and $d_r^{m,n}$) and its normalized power radiation pattern ($\xi_{m,n}$), with its phase adjusted by $\omega_{m,n}$ to ensure constructive interference at the receiver. According to [31], $\xi_{m,n}$ can be calculated from:

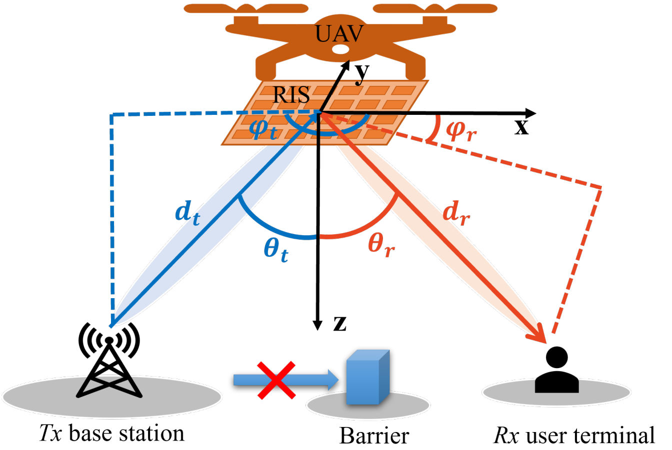

Fig. 2. Scene graph with geometric annotation of SBSU RIS-UAV mmWave communication system.

$$\begin{aligned} \xi_{m,n} &= (\cos\alpha_t^{m,n})^{\left(\frac{G_t}{2}-1\right)} \cos\theta_t^{m,n} \cos\theta_r^{m,n} (\cos\alpha_r^{m,n})^{\left(\frac{G_t}{2}-1\right)} \\ &= \left(\frac{(d_t)^2 + (d_t^{m,n})^2 - (d_{m,n})^2}{2 d_t d_t^{m,n}} \right)^{\left(\frac{G_t}{2}-1\right)} \frac{z_t}{d_t^{m,n}} \\ &\quad \times \frac{z_r}{d_r^{m,n}} \left(\frac{(d_r)^2 + (d_r^{m,n})^2 - (d_{m,n})^2}{2 d_r d_r^{m,n}} \right)^{\left(\frac{G_t}{2}-1\right)} \end{aligned}, \tag{2}$$

where $d_{m,n}$ is the Euclidean distance between U_0 and $U_{m,n}$.

B. SBSU Scenario

The RIS-UAV mmWave communication system under SBSU configuration is shown in Fig.1, where the LoS propagation between transceivers is obstructed by physical barriers, rendering direct communication infeasible. To address this limitation, the RIS-UAV platform is used to establish robust NLoS connectivity through precise phase compensation for incident mmWave signals, enabling directional reflection from the transmitter to the receiver. We assume that both the transmitting base station (Tx) and receiving user terminal (Rx) are in the far field of the RIS, and the peak radiation of both Tx and Rx point towards the center of RIS.

Because both the transmitting base station and receiving user terminal are in the far field of RIS, we can obtain the following relation:

$$\left\{\begin{array}{l}\cos\alpha_t^{m,n} = \cos\alpha_r^{m,n} \approx 1\\ \cos\theta_t^{m,n} \approx \cos\theta_t\\ \cos\theta_r^{m,n} \approx \cos\theta_r\end{array}\right. . \tag{3}$$

Then (2) can be rewritten as:

$$\xi_{m,n} = \cos\theta_t \cos\theta_r = \frac{z_t}{d_t}\frac{z_r}{d_r}. \tag{4}$$

To maximize the power of the receiving signal, the phase shift of $U_{m,n}$ can be configured as [30]:

$$\begin{array}{l}\omega_{m,n} = \bmod\left\{-\frac{2\pi}{\lambda}\left[\left(\sin\theta_t\cos\varphi_t + \sin\theta_r\cos\varphi_r\right)x_{m,n}\right.\right.\\ \left.\left.+ \left(\sin\theta_t\sin\varphi_t + \sin\theta_r\sin\varphi_r\right)y_{m,n}\right], 2\pi\right\}\end{array}, \tag{5}$$

where $x_{m,n}$ and $y_{m,n}$ are the X- and Y-coordinates of $U_{m,n}$. Then, the power received at Rx can be described as:

$$\begin{array}{l}P_r^{\mathrm{SISO}} \approx P_t\dfrac{G_tG_r\mu_x^2\mu_y^2A^2N^2M^2\cos\theta_t\cos\theta_r}{16\pi^2d_t^2d_r^2}\\ \qquad = P_t\dfrac{G_tG_r\mu_x^2\mu_y^2A^2N^2M^2z_tz_r}{16\pi^2(d_td_r)^3}\end{array} . \tag{6}$$

The aforementioned formulas are derived under the assumption that the RIS plane remains horizontal and stationary. However, since the RIS is integrated onto a UAV, in practical applications, the UAV's translation and rotation will affect signal propagation. Consequently, we will now explicitly analyze these dynamic effects, give the design of $\omega_{m,n}$ based on UAV movements and derive the corresponding expression for the received signal power.

1) UAV translation: Assuming the UAV undergoes translations d_x, d_y, and d_z along the X-, Y-, and Z-axes respectively, the updated coordinates of the RIS center and elements can be expressed as: $U_0^T(d_x,\ d_y,\ d_z)$. Then, the elevation angles and azimuth angles from the RIS center to the Tx/Rx antenna can be described as:

$$\left\{\begin{array}{l}\theta_{t/r}^{\mathrm{T}} = \arccos\left(\frac{z_{t/r}-d_z}{d_{t/r}^T}\right)\\ \varphi_{t/r}^{\mathrm{T}} = \arctan\left(\frac{y_{t/r}-d_y}{x_{t/r}-d_x}\right)\end{array}\right. , \tag{7}$$

where d_t^T and d_r^T represent the distance between the RIS center and Tx and Rx, respectively, after the translation of UAV. Then the configuration of the phase shift of the RIS elements could be uploaded based on $\theta_{t/r}^T$ and $\varphi_{t/r}^T$ from:

$$\begin{array}{l}\omega_{m,n}^T = \bmod\left\{-\frac{2\pi}{\lambda}\left[\left(\sin\theta_t^T\cos\varphi_t^T + \sin\theta_r^T\cos\varphi_r^T\right)x_{m,n}^T\right.\right.\\ \left.\left.+ \left(\sin\theta_t^T\sin\varphi_t^T + \sin\theta_r^T\sin\varphi_r^T\right)y_{m,n}^T\right], 2\pi\right\}\end{array}, \tag{8}$$

where $x_{m,n}^T$ and $y_{m,n}^T$ are the X- and Y-coordinates of RIS elements after translation. Finally, by importing (7) into (6), the received power can be written as:

$$\begin{array}{l}P_r^T \approx P_t\frac{G_tG_r\mu_x^2\mu_y^2A^2N^2M^2\cos\theta_t^{\mathrm{T}}\cos\theta_r^{\mathrm{T}}}{16\pi^2\left(d_t^Td_r^T\right)^2}\\ = P_t\frac{G_tG_r\mu_x^2\mu_y^2A^2N^2M^2(z_t-d_z)(z_r-d_z)}{16\pi^2\left(d_t^Td_r^T\right)^3},\\ \text{where}\quad d_t^T = \sqrt{\left(x_t-d_x\right)^2+\left(y_t-d_y\right)^2+\left(z_t-d_z\right)^2},\\ \text{and}\quad d_r^T = \sqrt{\left(x_r-d_x\right)^2+\left(y_r-d_y\right)^2+\left(z_r-d_z\right)^2}.\end{array} \tag{9}$$

2) UAV rotation: When the UAV rotates around the X, Y, and Z axes by angles σ_x, σ_y and σ_z respectively, corresponding rotation matrices can be established as follows:

$$\begin{array}{l}\mathbf{R_X}\left(\sigma_x\right) = \begin{bmatrix}1 & 0 & 0\\ 0 & \cos\sigma & -\sin\sigma\\ 0 & \sin\sigma & \cos\sigma\end{bmatrix},\\ \mathbf{R_Y}\left(\sigma_y\right) = \begin{bmatrix}\cos\sigma & 0 & \sin\sigma\\ 0 & 1 & 0\\ -\sin\sigma & 0 & \cos\sigma\end{bmatrix},\\ \text{and}\quad \mathbf{R_Z}\left(\sigma_z\right) = \begin{bmatrix}\cos\sigma & -\sin\sigma & 0\\ \sin\sigma & \cos\sigma & 0\\ 0 & 0 & 1\end{bmatrix}.\end{array} \tag{10}$$

By independently applying the above rotation matrices to the coordinates of Tx/Rx, the coordinates of Tx and Rx in the corresponding rotated coordinate system are calculated separately from:

$$\begin{array}{l}\nu_{\mathbf{X}}\left(\sigma\right) = \mathbf{R_X} \times \nu\\ = \left(x_{t/r}, y_{t/r}\cos\sigma - z_{t/r}\sin\sigma, y_{t/r}\sin\sigma + z_{t/r}\cos\sigma\right)^{\mathrm{T}},\\ \nu_{\mathbf{Y}}\left(\sigma\right) = \mathbf{R_Y} \times \nu\\ = \left(x_{t/r}\cos\sigma + z_{t/r}\sin\sigma, y_{t/r}, -x_{t/r}\sin\sigma + z_{t/r}\cos\sigma\right)^{\mathrm{T}},\\ \text{and}\quad \nu_{\mathbf{Z}}\left(\sigma\right) = \mathbf{R_Z} \times \nu\\ = \left(x_{t/r}\cos\sigma - \mathrm{y}_{t/r}\sin\sigma, x_{t/r}\sin\sigma + y_{t/r}\cos\sigma, z_{t/r}\right)^{\mathrm{T}}.\end{array} \tag{11}$$

where $\upsilon \in [(x_t, y_t, z_t)^T, (x_r, y_r, z_r)^T]$. Then, the corresponding elevation angles and azimuth angles from RIS center to Tx/Rx can be described as:

$$\begin{array}{l}\left\{\begin{array}{l}\theta_{t/r}^{R_X} = \arccos\left(\frac{y_{t/r}\sin\sigma + z_{t/r}\cos\sigma}{d_{t/r}}\right)\\ \varphi_{t/r}^{R_X} = \arctan\left(\frac{y_{t/r}\cos\sigma - z_{t/r}\sin\sigma}{x_{t/r}}\right)\end{array}\right.,\\ \left\{\begin{array}{l}\theta_{t/r}^{R_Y} = \arccos\left(\frac{-x_{t/r}\sin\sigma + z_{t/r}\cos\sigma}{d_{t/r}}\right)\\ \varphi_{t/r}^{R_Y} = \arctan\left(\frac{y_{t/r}}{x_{t/r}\cos\sigma + z_{t/r}\sin\sigma}\right)\end{array}\right.,\\ \text{and}\left\{\begin{array}{l}\theta_{t/r}^{R_Z} = \arccos\left(\frac{z_{t/r}}{d_{t/r}}\right)\\ \varphi_{t/r}^{R_Z} = \arctan\left(\frac{x_{t/r}\sin\sigma + y_{t/r}\cos\sigma}{x_{t/r}\cos\sigma - \mathrm{y}_{t/r}\sin\sigma}\right)\end{array}\right. .\end{array} \tag{12}$$

Then, the configuration of the phase shift of RIS elements could be uploaded based on the revised elevation/azimuth angles from (13). Finally, by independently substituting (12) into (6), the received power when the UAV rotates around the X, Y, and Z axes can be calculated respectively from (14). As demonstrated in (14), the variation in received signal power during UAV rotation about the X- or Y-axis is determined by both the rotation angle and the orthogonal spatial coordinates of the transceiver antennas (Y-coordinate for X-axis rotation

$$\begin{aligned}\omega_{m,n}^{R_X/R_Y/R_Y} &= \bmod\Big\{-\tfrac{2\pi}{\lambda}\Big[\Big(\sin\theta_t^{R_X/R_Y/R_Y}\cos\varphi_t^{R_X/R_Y/R_Y}+\sin\theta_r^{R_X/R_Y/R_Y}\cos\varphi_r^{R_X/R_Y/R_Y}\Big)x_{m,n}\\ &+\Big(\sin\theta_t^{R_X/R_Y/R_Y}\sin\varphi_t^{R_X/R_Y/R_Y}+\sin\theta_r^{R_X/R_Y/R_Y}\sin\varphi_r^{R_X/R_Y/R_Y}\Big)y_{m,n}\Big],2\pi\Big\}\end{aligned} . \tag{13}$$

$$\begin{cases} P_r^{R_X} \approx P_t\frac{G_tG_r\mu_x^2\mu_y^2A^2N^2M^2}{16\pi^2d_t^3d_r^3}\times\left(y_t\sin\sigma+z_t\cos\sigma\right)\left(y_r\sin\sigma+z_r\cos\sigma\right) = P_r^{\text{SISO}}\frac{(y_t\sin\sigma+z_t\cos\sigma)(y_r\sin\sigma+z_r\cos\sigma)}{z_tz_r}, \\ P_r^{R_Y} \approx P_t\frac{G_tG_r\mu_x^2\mu_y^2A^2N^2M^2}{16\pi^2d_t^3d_r^3}\times\left(-x_t\sin\sigma+z_t\cos\sigma\right)\left(-x_r\sin\sigma+z_r\cos\sigma\right) = P_r^{\text{SISO}}\frac{(-x_t\sin\sigma+z_t\cos\sigma)(-x_r\sin\sigma+z_r\cos\sigma)}{z_tz_r}, \\ \text{and}\quad P_r^{R_Z} \approx P_t\frac{G_tG_r\mu_x^2\mu_y^2A^2N^2M^2}{16\pi^2d_t^3d_r^3}z_tz_r = P_r^{\text{SISO}}. \end{cases} \tag{14}$$

$$\begin{cases} \omega_{(m,n)\in E_1}^{RX1} = \bmod\left\{-\frac{2\pi}{\lambda}\left[\left(\sin\theta_t\cos\varphi_t+\sin\theta_{r1}\cos\varphi_{r1}\right)x_{m,n}\right.\right. \left.\left. +\left(\sin\theta_t\sin\varphi_t+\sin\theta_{r1}\sin\varphi_{r1}\right)y_{m,n}\right],2\pi\right\} \\ \omega_{(m,n)\in E_2}^{Rx2} = \bmod\left\{-\frac{2\pi}{\lambda}\left[\left(\sin\theta_t\cos\varphi_t+\sin\theta_{r2}\cos\varphi_{r2}\right)x_{m,n}\right.\right. \left.\left. +\left(\sin\theta_t\sin\varphi_t+\sin\theta_{r2}\sin\varphi_{r2}\right)y_{m,n}\right],2\pi\right\} \end{cases} . \tag{15}$$

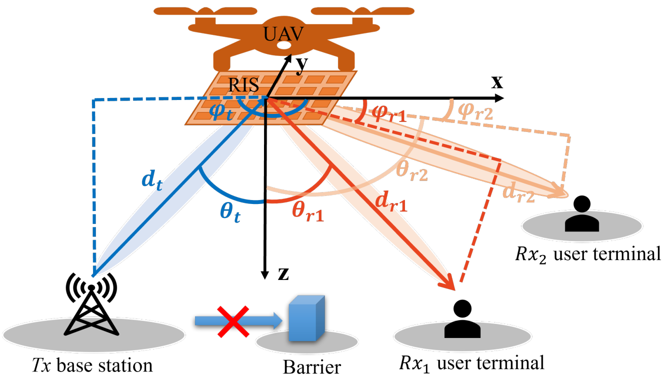

Fig. 3. Scene graph with geometric annotation of SBMU RIS-UAV mmWave communication system.

and X-coordinate for Y-axis rotation). In contrast, Z-axis rotation exhibits complete insensitivity in received power due to the constant elevation angle between the RIS center and transceiver antennas.

It is important to note that the preceding analyses considered UAV translation and rotation independently to clearly elucidate their distinct impacts on path loss and beam management. In practical flight scenarios, these movements are often coupled, meaning the RIS experiences simultaneous changes in both position and orientation. Modeling such coupled motion would involve applying combined transformation matrices, accounting for both translation vectors and rotation matrices like those in (10), to determine the instantaneous coordinates and effective pointing angles of each RIS element. While this increases the complexity of real-time channel parameter estimation and phase shift updates, the fundamental principles of phase compensation derived from our separate analyses remain critical building blocks for understanding and mitigating the impacts of these more complex dynamics. The established models for individual motion types provide a solid foundation for future investigations into coupled multi-degree-of-freedom UAV movements.

C. SBMU Scenario

Moving beyond the single-user case, we consider a 1×2 SBMU scenario, where a Tx base station delivers signals to two spatially separated receiving users (Rx_1 and Rx_2) via the joint RIS-UAV, as shown in Fig.3. To achieve simultaneous signal enhancement at both receivers, we propose the SDMA over RIS scheme: the RIS elements are equally divided into two independent subsets (E_1 and E_2), with their phase-shift configurations determined by the compensation principle from (15).

The equal partitioning of RIS elements into subsets E_1 and E_2 is adopted here for analytical tractability and to demonstrate the fundamental concept of SDMA over RIS. This approach is particularly effective when users have similar channel conditions or quality of service (QoS) requirements. However, in scenarios with significant asymmetry in user demands or channel qualities, a dynamic and unequal partitioning strategy could offer superior performance. For instance, allocating more elements to a user with poorer channel conditions or higher data rate requirements could enhance overall system fairness and throughput, albeit at the cost of increased complexity in element allocation optimization.

Assuming that the receiving gains of two users are the same, then the power received at Rx_1 and Rx_2 can be written as:

$$\begin{cases} P_{r1}^{\text{SIMO}} \approx P_t\frac{G_tG_r\mu_x^2\mu_y^2A^2\left(\frac{1}{2}NM\right)^2\cos\theta_t\cos\theta_{r1}}{16\pi^2d_t^2d_{r1}^2} \\ P_{r2}^{\text{SIMO}} \approx P_t\frac{G_tG_r\mu_x^2\mu_y^2A^2\left(\frac{1}{2}NM\right)^2\cos\theta_t\cos\theta_{r2}}{16\pi^2d_t^2d_{r2}^2} \end{cases} . \tag{16}$$

D. MBSU Scenario

To further explore system complexity involving multiple sources, the 2×1 MBSU configuration is investigated, as shown in Fig.4, where two spatially separated base stations (Tx_1 and Tx_2) communicate with a user terminal (Rx) via the RIS-UAV. Since RIS elements cannot simultaneously compensate for differential phase shifts of the signal from Tx_1 and Tx_2, effective methods should be adopted to solve this problem. Here, we propose two strategies: SDMA over RIS based on static UAV and MRUPC based on dynamic UAV.

1) SDMA over RIS based on static UAV: Analogously to SDMA over RIS scheme for phase difference compensation in the SBMU system, the static UAV scheme in the MBSU scenarios divides elements into two subsets dedicated to Tx_1 and Tx_2, with their configuration from (17). Then the received power can be modeled as (18), where P_r^{Tx1} and P_r^{Tx2} represent the received power from Tx_1 and Tx_2 to Rx, d_{t1} and

$$\left\{ \begin{array}{l} \omega^{Tx1}_{(m,n)\in E_1} = \mathrm{mod}\left\{-\frac{2\pi}{\lambda}\left[\left(\sin\theta_{t1}\cos\varphi_{t1}+\sin\theta_r\cos\varphi_r\right)x_{m,n} \quad +\left(\sin\theta_{t1}\sin\varphi_{t1}+\sin\theta_r\sin\varphi_r\right)y_{m,n}\right],2\pi\right\} \\ \omega^{Tx2}_{(m,n)\in E_2} = \mathrm{mod}\left\{-\frac{2\pi}{\lambda}\left[\left(\sin\theta_{t1}\cos\varphi_{t1}+\sin\theta_r\cos\varphi_r\right)x_{m,n} \quad +\left(\sin\theta_{t1}\sin\varphi_{t1}+\sin\theta_r\sin\varphi_r\right)y_{m,n}\right],2\pi\right\} \end{array} \right. . \tag{17}$$

$$\begin{aligned} P_r^{\text{static}} &= P_r^{Tx1}+P_r^{Tx2} \approx P_t\frac{G_tG_r\mu_x^2\mu_y^2A^2z_r}{16\pi^2d_r^3} \\ &\times\left(\begin{array}{l} \frac{z_{t1}}{d_{t1}^3}\left|\sum\limits_{(m,n)\in E_1} e^{-j\left(\frac{2\pi\left(d_{t1}^{m,n}+d_r^{m,n}\right)}{\lambda}-\omega_{m,n}^{Tx1}\right)}+\sum\limits_{(m,n)\in E_2} e^{-j\left(\frac{2\pi\left(d_{t1}^{m,n}+d_r^{m,n}\right)}{\lambda}-\omega_{m,n}^{Tx2}\right)}\right|^2 \\ +\frac{z_{t2}}{d_{t2}^3}\left|\sum\limits_{(m,n)\in E_1} e^{-j\left(\frac{2\pi\left(d_{t2}^{m,n}+d_r^{m,n}\right)}{\lambda}-\omega_{m,n}^{Tx1}\right)}+\sum\limits_{(m,n)\in E_2} e^{-j\left(\frac{2\pi\left(d_{t2}^{m,n}+d_r^{m,n}\right)}{\lambda}-\omega_{m,n}^{Tx2}\right)}\right|^2 \end{array}\right) \end{aligned} \tag{18}$$

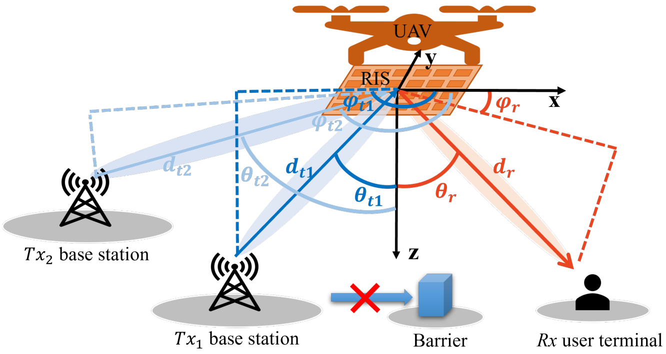

Fig. 4. Scene graph with geometric annotation of MBSU RIS-UAV mmWave communication system.

d_{t2} are the distances between RIS center and Tx_1 and Tx_2, respectively. However, this grouping strategy exhibits inherent limitations in phase compensation: RIS elements serving Tx_1 cannot provide a precise phase correction for Tx_2 signals, and vice versa. To address these phase compensation conflicts in the static UAV scheme, we propose the MRUPC scheme based on dynamic UAV.

2) *MRUPC based on dynamic UAV:* The MRUPC based on dynamic UAV leverages the mobility of UAV-RIS to reduce the demand for precise phase design of RIS elements. Specifically, by moving the UAV, the elevation and azimuth angles of the signals arriving at the center of the RIS from Tx_1 and Tx_2 can be made identical. Consequently, the required phase compensation factor $\omega_{m,n}$ becomes the same for both transmitters. This collaborative dynamic optimization eliminates the need to divide the RIS elements into two groups to separately compensate for the phase differences caused by Tx_1 and Tx_2, thus improving the received power. The implementation process of MRUPC strategy includes the following three steps.

Step 1: Calculate the optimal coordinates of RIS Let Tx_1, Tx_2, and Rx coordinates be (x_{t1}, y_{t1}, z_{t1}), (x_{t2}, y_{t2}, z_{t2}) and (x_r, y_r, z_r), respectively, with RIS initially centered at U_0 (0, 0, 0) and optimized position U_0' (x_u, y_u, z_u), which satisfy spatial constraints $x_{t2} < x_{t1} < x_u < x_r$ and $z_u < z_{t1} < z_{t2}$. To ensure that the elevation and azimuth angles of RIS to Tx_1 and Tx_2 are the same, we assume that the UAV-RIS moves to a position collinear with Tx_1 and Tx_2. Therefore, after the movement, the center point of the RIS, denoted as U_0', can be expressed as:

$$\left\{ \begin{array}{l} x_u = x_{t2} + k\left(x_{t1}-x_{t2}\right) \\ y_u = y_{t2} + k\left(y_{t1}-y_{t2}\right) \\ z_u = z_{t2} + k\left(z_{t1}-z_{t2}\right) \end{array} \right. , \tag{19}$$

where k >0 is the regulatory parameter. For maintaining the far-field conditions between the transmitting antenna and RIS, the distance from the transmitting antenna to the center of the RIS must be no less than $2\mu_x\mu_yMN/\lambda$ [30]. Consequently, we can derive the following relationship:

$$\sqrt{\left(x_u-x_{t1}\right)^2+\left(y_u-y_{t1}\right)^2+\left(z_u-z_{t1}\right)^2} \geq \frac{2\mu_x\mu_yMN}{\lambda}. \tag{20}$$

Substituting (20) into (19) and simplifying, the constraint for k can be obtained from:

$$k \geq \frac{2\mu_x\mu_yMN}{\lambda d_{t1t2}}+1, \tag{21}$$

where d_{t1t2} represents the distance between Tx_1 and Tx_2.

Step 2: UAV repositioning and angle calculation

Let UAV moves to the coordinate position determined by (19), then the new elevation and azimuth angles from the RIS center to Tx_1 and Tx_2 become identical, which can be described as:

$$\left\{ \begin{array}{l} \theta_{t/r}^D = \arccos\left(\frac{z_{t/r}-z_u}{d_{t/r}^T}\right) \\ \varphi_{t/r}^D = \arctan\left(\frac{y_{t/r}-y_u}{x_{t/r}-x_u}\right) \end{array} \right. . \tag{22}$$

Step 3: Phase compensation design

Since the elevation and azimuth angles from the RIS center to the two base stations have become identical, we can apply the same phase compensation coefficients to beamform the signals from base stations Tx_1 and Tx_2. The phase compensation design is given by the following formula:

$$\begin{aligned} \omega_{m,n}^D = \mathrm{mod}&\left\{-\frac{2\pi}{\lambda}\left[\left(\sin\theta_t^D\cos\varphi_t^D+\sin\theta_r^D\cos\varphi_r^D\right)x_{m,n}^D\right.\right. \\ &\left.\left.+\left(\sin\theta_t^D\sin\varphi_t^D+\sin\theta_r^D\sin\varphi_r^D\right)y_{m,n}^D\right],2\pi\right\}, \end{aligned} \tag{23}$$

where $x_{m,n}^D$ and $y_{m,n}^D$ are the X- and Y-coordinates of RIS elements after moving.

The MRUPC eliminates the need to divide the RIS elements into two groups for separate design. As a result, all RIS

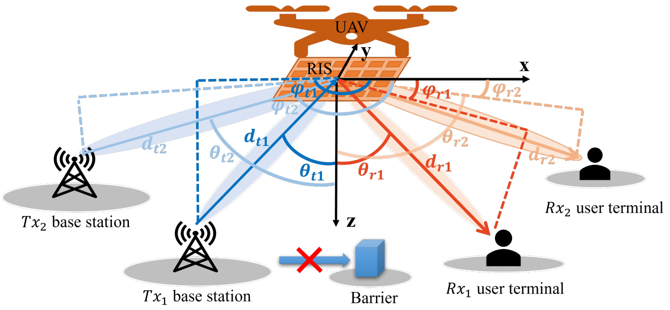

Fig. 5. Scene graph with geometric annotation of MBMU RIS-UAV mmWave communication system.

elements can be utilized to reflect the signals from both transmitting antennas toward the receiving antenna. Then, the power received at Rx can be expressed as follows:

$$\begin{aligned} & P_r^{\text{dynamic}} = P_r^{Tx1} + P_r^{Tx2} \\ & \approx P_t \frac{G_t G_r \mu_x^2 \mu_y^2 A^2 N^2 M^2 (z_r - z_u)}{16\pi^2 \left(d_r'\right)^3} \times \left(\frac{z_{t1} - z_u}{\left(d_{t1}'\right)^3} + \frac{z_{t2} - z_u}{\left(d_{t2}'\right)^3} \right) , \end{aligned} \tag{24}$$

where d_r', d_{t1}', and d_{t2}' are the distances between U_0' to Rx, U_0' to Tx_1, and U_0' to Tx_2, respectively.

E. MBMU Scenario

In practical applications, due to limitations such as the operational ceiling, battery life, no-fly zones, or physical obstacles, the UAV may not be able to reach the optimal position described by (19). The key idea of MRUPC is to find a position that equalizes the arrival angles from different base stations. If perfect collinearity is not feasible, the UAV could be positioned to minimize the difference in arrival angles, thereby reducing the impact of phase compensation conflicts on system performance as much as possible.

Building upon the previous analyses of multi-user terminal or multi-base station configurations, finally, the path-loss model is extended to a 2x2 MBMU scenario, as illustrated in Fig. 5. In this setup, two spatially distinct transmitting base stations (Tx_1 and Tx_2) send signals to two different receiving user terminals (Rx_1 and Rx_2) via an RIS-UAV. This MBMU scenario can be considered a combination of SBMU and MBSU scenarios. Therefore, we integrate the SDMA over RIS scheme from the SBMU context with the MRUPC from the MBSU context. Initially, the optimal position for the RIS based on the locations of Tx_1 and Tx_2 is calculated. Then the UAV is moved so that the elevation/azimuth angles from the center of the RIS to Tx_1 and Tx_2 are identical. Following this adjustment, the RIS elements are evenly divided into two groups, each dedicated to reflecting signals towards Rx_1 and Rx_2, respectively, with their phase shift configured from:

$$\left\{ \begin{aligned} & P_{r1}^{MIMO} \approx P_t \frac{G_t G_r \mu_x^2 \mu_y^2 A^2 \left(\frac{1}{2} NM\right)^2 (z_{r1} - z_u)}{16\pi^2 \left(d_{r1}'\right)^3} \\ & \times \left(\frac{z_{t1} - z_u}{\left(d_{t1}'\right)^3} + \frac{z_{t2} - z_u}{\left(d_{t2}'\right)^3} \right) \\ & P_{r2}^{MIMO} \approx P_t \frac{G_t G_r \mu_x^2 \mu_y^2 A^2 \left(\frac{1}{2} NM\right)^2 (z_{r2} - z_u)}{16\pi^2 \left(d_{r2}'\right)^3} \\ & \times \left(\frac{z_{t1} - z_u}{\left(d_{t1}'\right)^3} + \frac{z_{t2} - z_u}{\left(d_{t2}'\right)^3} \right) \end{aligned} \right. . \tag{25}$$

Consequently, the received signal power at Rx_1 and Rx_2 can be expressed as (26).

III. NUMERICAL SIMULATION RESULTS AND DISCUSSIONS

To validate the derived models and evaluate the proposed strategies across these diverse scenarios, based on the unified channel model and the different phase compensation schemes established in Section II, we conduct numerical simulations for RIS-UAV mmWave communication systems under different scenarios. By comparing simulation results with derived analytical expressions of received power across SBSU, SBMU, MBSU, and MBMU scenarios, we validate the reliability and universality of our modeling framework in different scenarios.

Under ideal conditions, RIS can effectively diffract/refract mmWave to achieve NLoS communication. Combined with the advantages of flexible deployment of UAV, it is expected to significantly expand the application boundaries of mmWave communication. However, in actual deployment, the wavelength of mmWave communication signals is short and extremely sensitive to changes in the position of RIS. UAVs will be affected by wind, air pressure, mechanical vibration, etc. during suspension, and experience rapid attitude changes, body vibration and other factors, which will cause physical disturbances on the RIS panel and further generate phase control errors.

Therefore, in this section, we analyze the attitude of RIS-UAV in static and dynamic conditions, especially the impact of small translation and rotation on the communication link. Critical simulation parameters and scenario-specific power calculation models are detailed in Table I (system parameters) and Table II (scenario-formula mapping).

A. Results of SBSU Scenario

First, we conducted simulations and calculations to analyze the variation of received signal power at Rx under the SBSU scenario with a static UAV, as functions of the transmission distance d_t and reflection distance d_r. As shown in Fig. 6(a),

$$\left\{ \begin{aligned} \omega_{(m,n)\in E_1}^{RX1} &= \bmod \left\{ -\frac{2\pi}{\lambda} \left[\left(\sin\theta_t^D \cos\varphi_t^D + \sin\theta_{r1}^D \cos\varphi_{r1}^D \right) x_{m,n}^D + \left(\sin\theta_t^D \sin\varphi_t^D + \sin\theta_{r1}^D \sin\varphi_{r1}^D \right) y_{m,n}^D \right], 2\pi \right\} \\ \omega_{(m,n)\in E_2}^{Rx2} &= \bmod \left\{ -\frac{2\pi}{\lambda} \left[\left(\sin\theta_t^D \cos\varphi_t^D + \sin\theta_{r2}^D \cos\varphi_{r2}^D \right) x_{m,n}^D + \left(\sin\theta_t^D \sin\varphi_t^D + \sin\theta_{r2}^D \sin\varphi_{r2}^D \right) y_{m,n}^D \right], 2\pi \right\} \end{aligned} \right. . \tag{26}$$

TABLE I
SYSTEM PARAMETERS

Parameter name	Symbol	Value
Output power	P_t	0 dbm
Gain of the transmitting antenna	G_t	21 dB
Gain of the receiving antenna	G_r	21 dB
Signal frequency	f	10.5 GHz
Light speed	c	3 × 108 m/s
Signal wavelength	$\lambda = c/f$	0.0286 m
RIS elements width	u_x	0.01 m
RIS elements length	u_y	0.01 m
Number of columns of RIS elements	N	102
Number of rows of RIS elements	M	100
Reflection amplitude of RIS elements	A	0.9

TABLE II
POWER CALCULATION MODEL FOR DIFFERENT SCENARIOS

Scenario	Phase design	Power calculation model	Notes
SBSU	(5) for static UAV; (8) for translatory UAV; (13) for rotary UAV	(6) for static UAV; (9) for translatory UAV; (14) for rotary UAV	θ_t = 45°, φ_t = 180°, d_t = 80 m; θ_r = 45°, φ_r = 0°, d_r = 80 m.
SBMU	(15)	(16)	θ_t = 45°, φ_t = 180°, d_t = 80 m; θ_{r1} = 45°, φ_{r1} = 0°, d_{r1} = 80 m; θ_{r2} = 60°, φ_{r1} = 60°, d_{r2} = 80 m.
MBSU	(17) for static UAV; (23) for dynamic UAV	(18) for static UAV; (24) for dynamic UAV	θ_{t1} = 45°, φ_{t1} = 180°, d_{t1} = 80 m; θ_{t2} =45.8°, φ_{t2}=166.6°, d_{t2} = 80 m; θ_r = 45°, φ_r = 0°, d_r = 80 m.
MBMU	(25)	(26)	θ_{t1} = 45°, φ_{t1} = 180°, d_{t1} = 80 m; θ_{t2} =45.8°, φ_{t2}=166.6°, d_{t2} = 80 m; θ_{r1} = 45°, φ_{r1} = 0°, d_{r1} = 80 m; θ_{r2} = 60°, φ_{r1} = 60°, d_{r2} = 80 m.

solid lines represent the received power calculated using (6), while dashed lines correspond to simulation results based on the RIS phase distribution designed via (5). The close agreement between theoretical calculations and simulations validates the correctness of the derived equations and the effectiveness of the RIS phase design. Additionally, the received power at Rx decreases monotonically with increasing d_t or d_r, consistent with the inverse relationship between Pr and d_t d_r as defined in (6). Fig. 6(b) illustrates the signal strength distribution when d_t = 80 m and d_r = 80 m. The results demonstrate that the signal strength peaks at Rx (θ_r = 45°, φ_r = 0°) with a power of -60.1 dBm, indicating that signals from the Tx are effectively reflected to Rx via RIS. This further substantiates the reliability of the RIS phase design.

Building on the analysis of the static UAV, we then investigated the impact of UAV translation along the X, Y, and Z axes on the received power at Rx. As shown in Fig. 7(a), solid lines represent theoretical results calculated using (9), while dashed lines correspond to simulation results based on (8). Notably, the theoretical and simulated trends align closely, with a minor discrepancy of approximately 0.2 dBm in magnitude. This deviation arises from the approximation assumptions in (3), which simplifies the effect of normalized power radiation patterns ($\xi_{m,n}$) on received power, leading to a slight overestimation in theoretical calculations. In addition, significant variations in received power occur when the UAV translates along the Y or Z axes, whereas negligible changes are observed during the X-axis translation. This behavior is attributed to the system's geometric symmetry: The Tx-Rx link exhibits Y-axis symmetry, making the product dtdr quasi-invariant during X-axis displacement, resulting in minimal impact on received power. Figs. 7(b), (c), and (d) illustrate the signal energy distribution after translating the UAV by 10 m along the X, Y, and Z axes, respectively. The results demonstrate that signals from Tx are effectively steered to Rx even under UAV translation by dynamically updating the RIS phase distribution. This outcome underscores the robustness of the proposed RIS phase adjustment strategy, which maintains stable signal delivery despite channel variations caused by UAV motion.

Next, we further investigated the impact of UAV rotation on received power. As shown in Fig. 8(a), solid lines represent theoretical results calculated using (14), while dashed lines correspond to simulation results based on (13). Notably, the theoretical and simulated trends align closely, with a consistent 0.2 dBm discrepancy in magnitude, arising from the same reason as in the translation scene. As observed in Fig. 8(a), minor fluctuations in received power occur when the UAV rotates around the X or Y axes, whereas negligible changes are observed during the Z-axis rotation. This behavior is due to the geometric invariance during Z-axis rotation, where the elevation angles and distances between the RIS and both Tx/Rx remain unchanged, resulting in no significant impact on received energy. To evaluate system robustness under rotations, Figs. 8(b), (c), and (d) illustrate the signal power distribution after rotating the UAV by 10° around the X, Y, and Z axes, respectively. The results demonstrate that signals from Tx are effectively steered to Rx even under UAV rotation by dynamically updating the RIS phase distribution. This outcome highlights the adaptability of the proposed RIS phase adjustment strategy, which maintains stable power transmission despite spatial misalignment caused by UAV rotation.

B. *Results of SBMU Scenario*

We next examined the received signal power at Rx_1 and Rx_2 under a 1×2 SBMU configuration as functions of the d_t and d_r. As shown in Fig. 9(a), solid lines represent theoretical results calculated using (16), while dashed lines correspond to simulation results based on (15). Notably, the theoretical and simulated trends align closely, with both Rx_1 and Rx_2 exhibiting decreasing received power as d_t or d_r increases, consistent with the inverse relationship observed in SBSU scenarios. Further observation reveals that Rx_1 receives slightly higher power than Rx_2, despite their equal distances to the RIS. This disparity arises from the smaller elevation angle (θ_{r1})

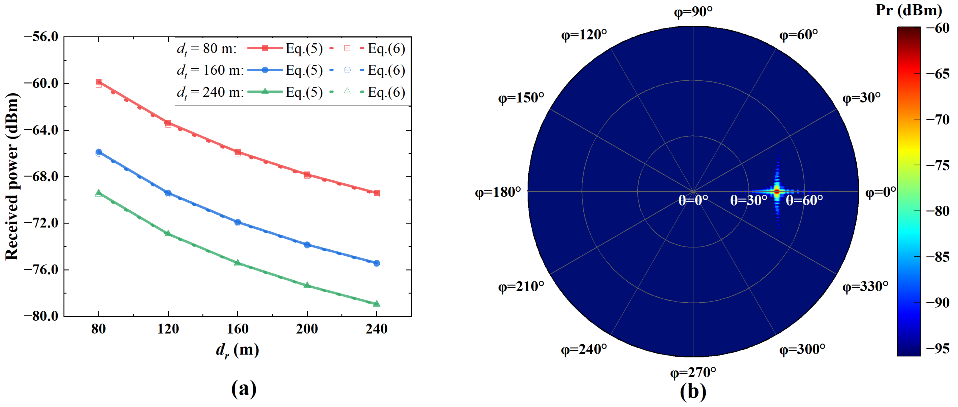

Fig. 6. Numerical simulation results of SBSU UAV-RIS mmWave communication system: (a) Received signal power at Rx (θ_r = 45°, φ_r = 0°) versus different d_t and d_r, and (b) received signal power distribution when d_t = 80 m and d_r = 80 m.

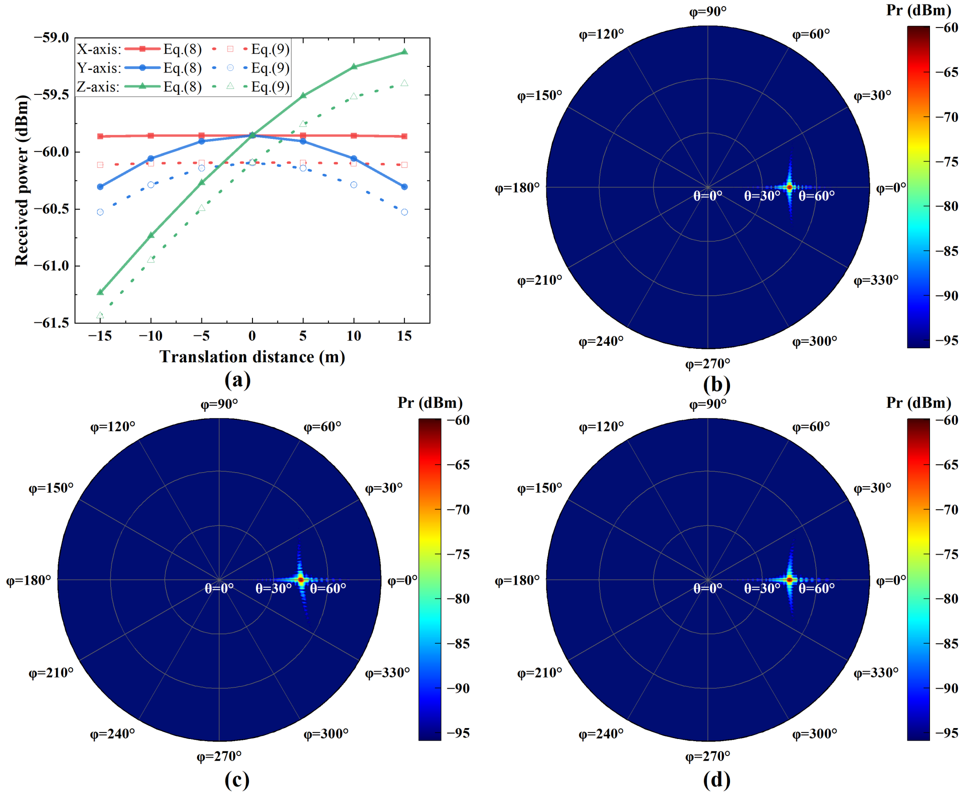

Fig. 7. Numerical simulation results of translatory UAV: (a) Received power versus different translation distances and received signal power distribution when UAV translates 10 m along (b) X-axis, (c) Y-axis and (d) Z-axis.

of Rx_1 relative to Rx_2 (θ_{r2}), which enhances the normalized power radiation pattern gain at Rx_1, thereby increasing its received power. To validate the effectiveness of the proposed RIS-SDMA in multi-receiver scenarios, Fig. 9(b) illustrates the signal power distribution when d_t = 80 m and d_r = 80 m. The results show significant power concentration at Rx_1 (θ_{r1} = 45°, φ_{r1} = 0°) and Rx_2 (θ_{r2} = 60°, φ_{r1} = 60°), demonstrating that signals from Tx are simultaneously steered to both Rx_1 and Rx_2 via a single RIS. Furthermore, the received power at Rx_1 is measured as -66.2 dBm, approximately one-quarter of the SBSU scenario power, aligning with the theoretical calculations in Eqs. (5) and (16). This validates the rationality of power distribution in multi-receiver configurations.

To further validate the scalability of our proposed SDMA over RIS scheme in scenarios with more users, we extend the simulation to a four-user case, with the resulting received signal energy distribution shown in Fig. 9(c). The figure demonstrates that when the RIS serves four users simultaneously, the system can successfully generate four distinct beams, with energy peaks precisely aligned with the intended user locations. This provides strong evidence that our approach can be effectively scaled to support a larger user base. It is worth noting that the peak energy for each user in the four-user case, as seen in Fig. 9(c), is lower than that in the two-

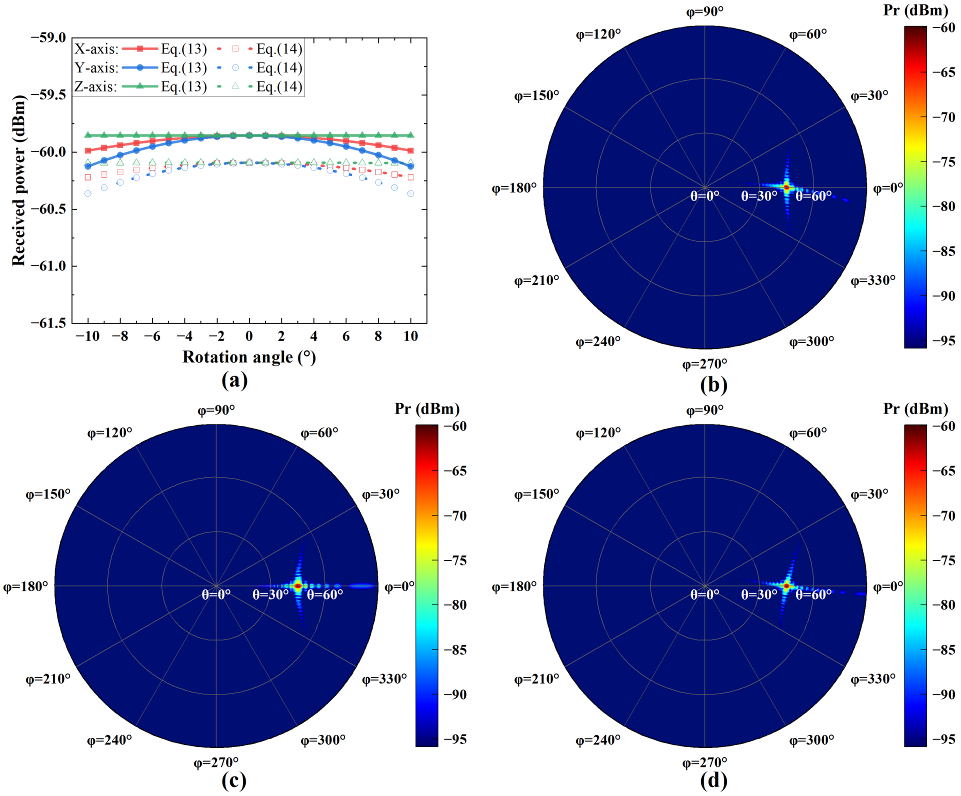

Fig. 8. Numerical simulation results of rotary UAV: (a) Received power versus different translation distances and received signal power distribution when UAV rotates 10° around (b) X-axis, (c) Y-axis and (d) Z-axis.

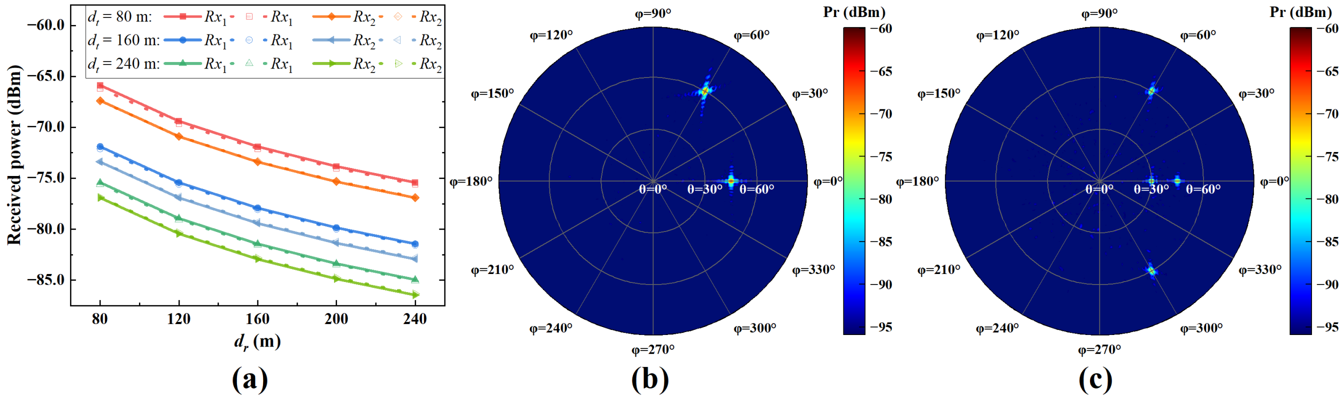

Fig. 9. Numerical simulation results of SBMU UAV-RIS mmWave communication system: (a) Received signal power at Rx_1 (θ_{r1} = 45°, φ_{r1}= 0°) and Rx_2 (θ_{r2} = 60°, φ_{r2} = 60°) versus different d_t and d_r, and received signal power distribution when d_t = 80 m and d_r = 80 m for (b) two users including Rx_1 and Rx_2 and for (c) four users including Rx_1, Rx_2, Rx_3 (θ_{r3} = 30°, φ_{r3}= 0°), and Rx_4 (θ_{r4} = 60°, φ_{r4}= 300°).

user scenario shown in Fig. 9(b). This reduction is a direct consequence of partitioning the total RIS aperture into four smaller subsets, which diminishes the reflective gain allocated to each individual user. This trade-off between per-user gain and the number of supported users is an inherent characteristic of RIS-based SDMA schemes.

C. Results of MBSU Scenario

Then, we evaluated the performance of the proposed beam management schemes in the 2×1 MBSU setup. As shown in Fig. 10, by adjusting the position of Tx_2 (with its X-coordinate always smaller than Tx_1), we quantified the impact of the distance between Tx_1 and Tx_2 (d_{t1t2}) on received signal power. Notably, the red and blue lines correspond to measured results under dynamic and static UAV schemes, respectively. Solid lines represent theoretical results calculated using (24) and (18), while dashed lines correspond to simulations based on (23) and (17). The results demonstrate a close agreement between theoretical and simulation values, with the dynamic UAV scheme outperforming the static counterpart by 7.9 dBm and 6.4 dBm when d_{t1t2} = 30 m and 90 m, respectively. The reduction in relative gain of received power is primarily due

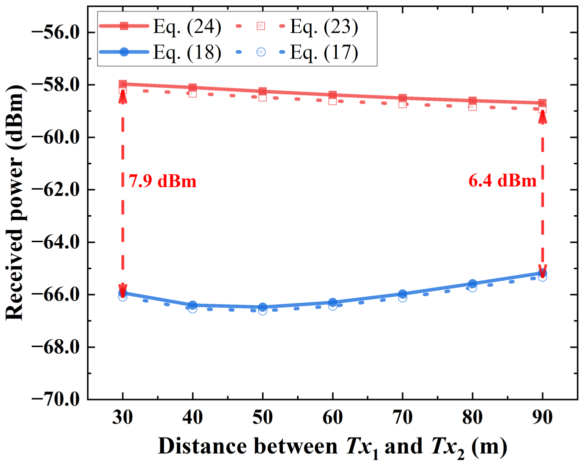

Fig. 10. Received signal power at Rx (θ_r = 45°, φ_r = 0°) versus different d_{t1t2} under static and dynamic UAV schemes.

to the fact that, in the MRUPC scheme, the received power decreases as d_{t1t2} increases, whereas in the static scheme, the received power slightly increases. For MRUPC, as d_{t1t2} grows, the UAV's optimal position U_0' (determined by (19) and (21)) moves farther away from Tx_1 and Tx_2, increasing the path loss from both transmitters to the RIS. This leads to a gradual decline in the received power under the MRUPC scheme, as shown by the red curve in Fig.10. In contrast, for the static scheme, as d_{t1t2} increases, the angular difference between the RIS and Tx_1/ Tx_2 (in terms of elevation and azimuth) decreases, causing scattered energy from phase mismatches to converge more toward the receiver, thereby enhancing the received power. Nevertheless, MRUPC still outperforms the static scheme by achieving a higher overall received power.

To visualize power distribution characteristics, Figs. 12 and 13 illustrate the signal power distribution when d_{t1t2} = 30 m and 90 m, respectively. The results show that under the dynamic scheme, signals from both Tx_1 and Tx_2 are effectively steered to Rx (θ_r = 45°, φ_r = 0°), forming concentrated power. In contrast, the static scheme fails to simultaneously align Tx_1 and Tx_2 phase shifts, leading to scattered power. Notably, comparing Figs. 12(a-c) and 13(a-c), scattered power gradually shifts toward Rx as d_{t1t2} increases, further explaining the increasing power observed in the static scheme at larger distances.

D. Results of MBMU Scenario

Finally, we evaluated the system performance in the 2×2 MBMU setup. Similar to the 2×1 MBSU scenario, we fixed Tx_1 and adjusted Tx_2's position while employing the dynamic UAV scheme exclusively. As shown in Fig. 11, solid lines represent theoretical results calculated using (26), while dashed lines correspond to simulations based on (25). Red and blue lines denote received energy at Rx_1 and Rx_2, respectively. The results demonstrate a close agreement between theoretical and simulation values, with the received power at Rx_1 following a trend consistent with the MBSU configuration as d_{t1t2} (the distance between Tx_1 and Tx_2) varies. Notably, the received power at Rx_2 exhibits minimal variation with d_{t1t2}. This behavior is attributed to the adaptive adjustment of the dynamic UAV scheme: as d_{t1t2} increases, the UAV moves closer to Rx_2, reducing power loss from the RIS to Rx_2 and offsetting signal attenuation caused by Tx_2's increasing distance from the RIS. To validate multi-antenna beamforming capability, Fig. 11(b) illustrates the signal power distribution. The results show that signals from both Tx_1 and Tx_2 are effectively steered to Rx_1 (θ_{r1} = 45°, φ_{r1} = 0°) and Rx_2 (θ_{r2} = 60°, φ_{r1} = 60°) forming dual-beam focusing. This demonstrates the proposed MRUPC scheme's ability to achieve precise directional signal transmission for multiple users in MBMU configurations, confirming its universality across complex communication architectures.

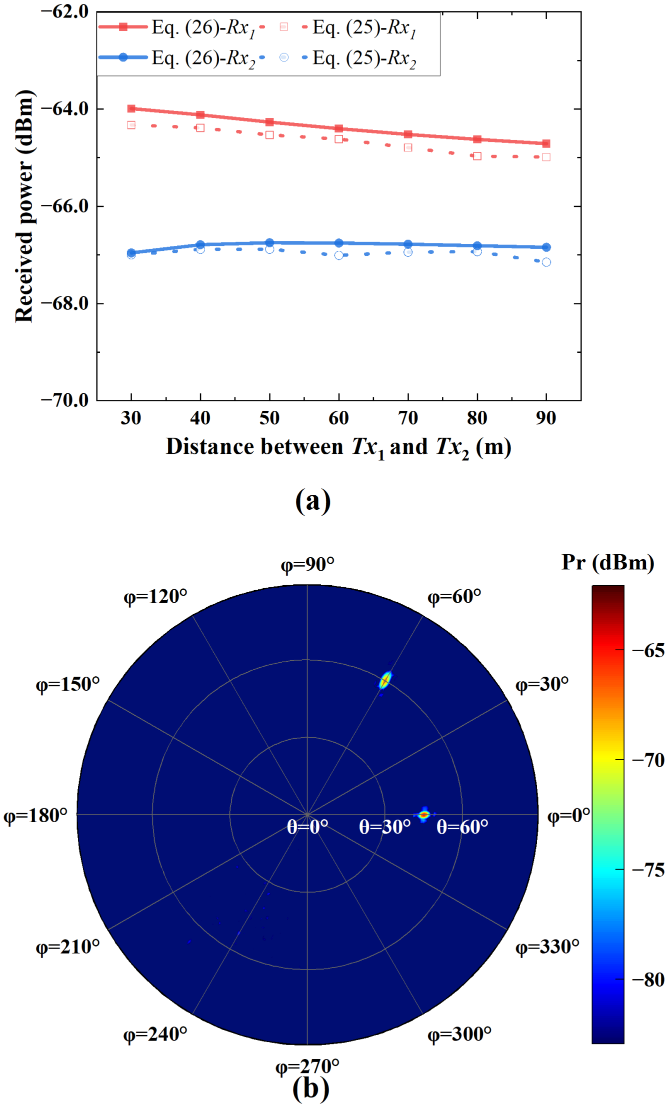

Fig. 11. Numerical simulation results of MBMU UAV-RIS mmWave communication system: (a) Received signal power at Rx_1 (θ_{r1} = 45°, φ_{r1} = 0°) and Rx_2 (θ_{r2} = 60°, φ_{r1} = 60°) versus different d_{t1t2} and (b) received signal power distribution when d_{t1t2} = 90 m.

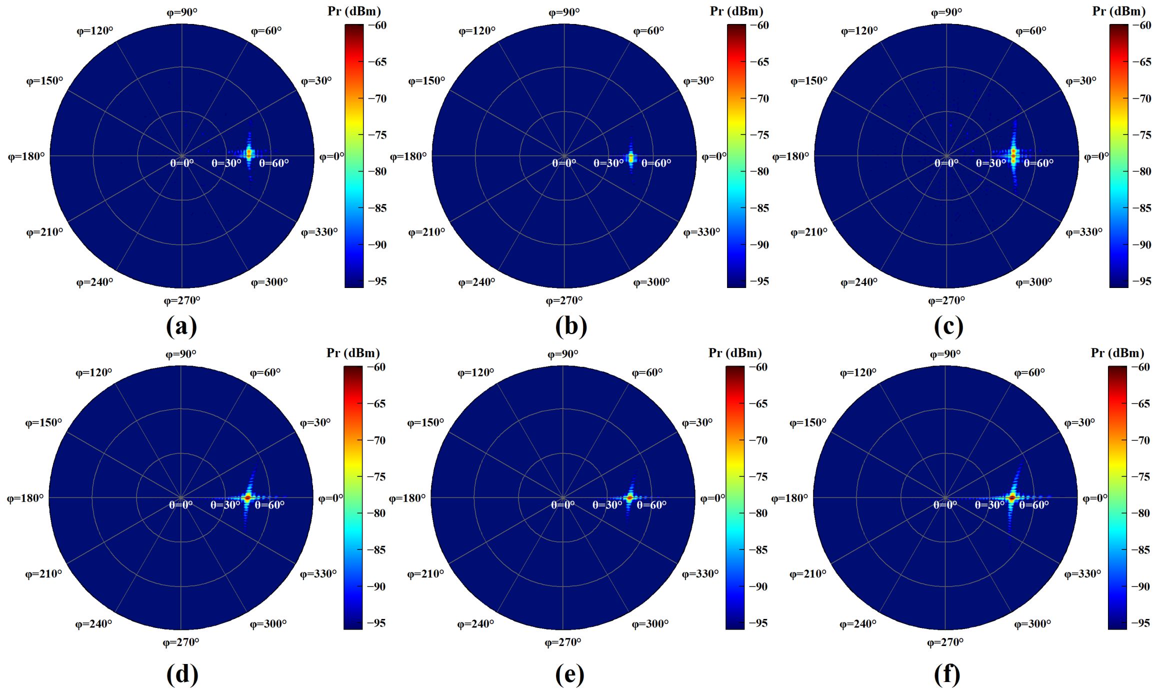

Fig. 12. Received signal power distribution when d_{t1t2} = 30 m: (a) signal coming from Tx_1, (b) signal coming from Tx_2 and (c) the combined signal of Tx_1 and Tx_2 when adopting static UAV scheme; (d) signal coming from Tx_1, (e) signal coming from Tx_2 and (f) the combined signal of Tx_1 and Tx_2 when adopting dynamic UAV scheme.

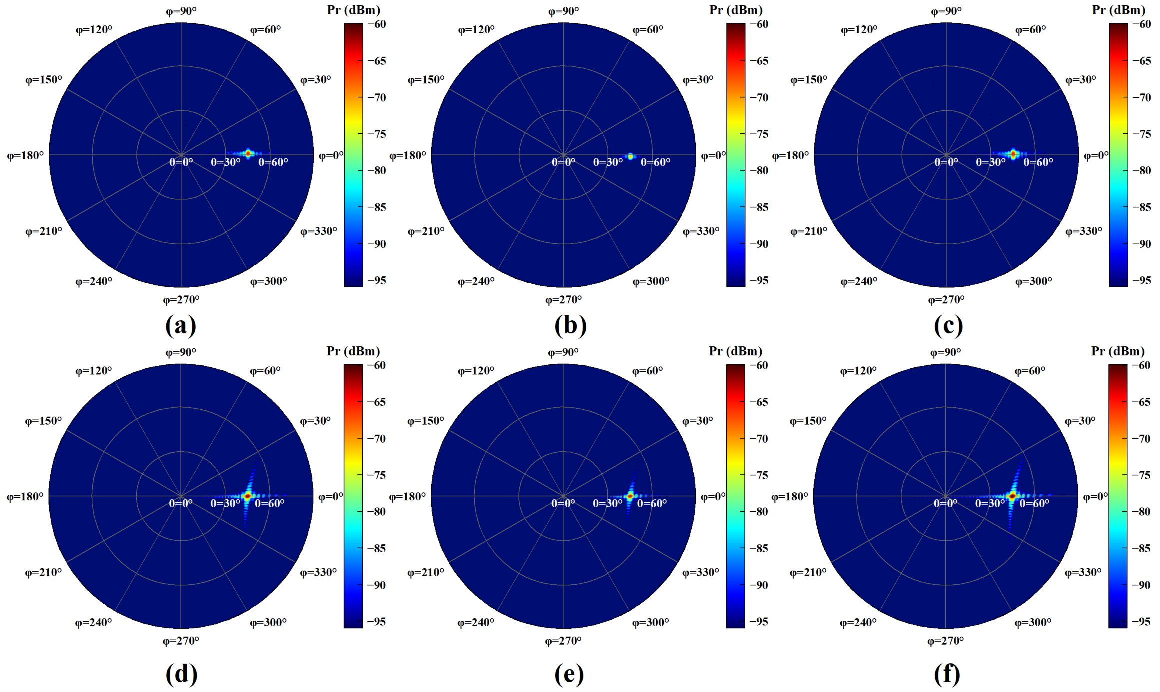

Fig. 13. Received signal power distribution when d_{t1t2} = 30 m: (a) signal coming from Tx_1, (b) signal coming from Tx_2 and (c) the combined signal of Tx_1 and Tx_2 when adopting static UAV scheme; (d) signal coming from Tx_1, (e) signal coming from Tx_2 and (f) the combined signal of Tx_1 and Tx_2 when adopting dynamic UAV scheme.

IV. CONCLUSION

In the B5G/6G era, RIS-UAV is an important means to build flexible and controllable aerial base stations or relay nodes, which can achieve efficient and on-demand millimeter wave coverage, especially in emergency, disaster and temporary assembly scenarios. This paper numerically simulates the RIS-UAV assisted mmWave communication systems across diverse scenarios from SBSU to MBMU, aiming to address limitations in unified cross-scenario analysis, modeling of UAV dynamics, multi-user access efficiency, and multi-base station coordination capabilities in existing research. Only by understanding the impact of UAV motion and vibration on mmWave communication links can we realize a usable, reliable, and mass-produced RIS aerial platform in the future. Thus, we establish the path loss model considering UAV translation and rotation, propose a SDMA over RIS scheme via RIS element partitioning, and pioneer a MRUPC strategy leveraging UAV mobility. The results confirm the accuracy of our models, quantify the effects of UAV dynamics, demonstrate the effectiveness of SDMA over RIS scheme in supporting multiple users, and critically verify that the MRUPC strategy yields significant performance gains (approx. 6-8 dB) over static UAV schemes employing SDMA in multi-base station scenarios, highlighting the substantial potential of exploiting UAV mobility to overcome coordination challenges. The main contributions lie in providing the first systematic cross-scenario analytical framework, the multi-user access mechanism, and the multi-base station coordination strategy, offering essential theoretical foundations and practical guidance for designing more robust and efficient RIS-UAV mmWave systems.

Building upon the systematic framework established in this paper, several promising avenues for future research emerge. First, our current analysis focuses on macro-scale UAV movements. A significant extension would be to incorporate the impact of micro-dynamic effects, such as high-frequency UAV vibrations and wind-induced turbulence, on the precision of RIS phase control and overall channel stability. This would necessitate the development of more sophisticated stochastic channel models. Furthermore, this work adopted a simplified equal partitioning for the SDMA over RIS scheme. Future studies should therefore explore dynamic and optimized RIS partitioning strategies, potentially leveraging iterative algorithms or machine learning techniques. Such strategies would be crucial for adapting to heterogeneous channel conditions and diverse Quality of Service (QoS) requirements, thereby enhancing overall system throughput and fairness.

APPENDIX

PROF OF FORMULA (14)

By substituting the elevation and azimuth angles from the RIS (after rotating the UAV by angle σ around the X-axis) to the base station and the user, as shown in (12), into the received signal power expression in (6), we obtain the new energy expression as follows:

$$
\begin{aligned}
&P_r^{\mathrm{R}_X} \approx P_t \frac{G_t G_r \mu_x^2 \mu_y^2 A^2 N^2 M^2}{16\pi^2 d_t^2 d_r^2} \cos\left[\arccos\left(\frac{y_t \sin\sigma + z_t \cos\sigma}{d_t}\right)\right] \\
&\times \cos\left[\arccos\left(\frac{y_r \sin\sigma + z_r \cos\sigma}{d_r}\right)\right] \\
&= P_t \frac{G_t G_r \mu_x^2 \mu_y^2 A^2 N^2 M^2}{16\pi^2 (d_t d_r)^2} \left(\frac{y_t \sin\sigma + z_t \cos\sigma}{d_t}\right) \left(\frac{y_r \sin\sigma + z_r \cos\sigma}{d_r}\right) \\
&= P_t \frac{G_t G_r \mu_x^2 \mu_y^2 A^2 N^2 M^2}{16\pi^2 (d_t d_r)^3} \left(y_t \sin\sigma + z_t \cos\sigma\right) \\
&\times \left(y_r \sin\sigma + z_r \cos\sigma\right).
\end{aligned}
$$

Then, by substituting (6) into above formula, we can obtain the received power expression for the UAV rotate around the X-axis as:

$$
P_r^{\mathrm{R}_X} = P_r^{SISO} \frac{\left(y_t \sin\sigma + z_t \cos\sigma\right)\left(y_r \sin\sigma + z_r \cos\sigma\right)}{z_t z_r}.
$$

Similarly, by substituting the elevation and azimuth angles from the RIS (after rotating the UAV by angle A around the Y-axis or Z-axis), as expressed in (12), into (6), and then simplifying the resulting expressions, we obtain the corresponding energy expressions as follows:

$$
\begin{aligned}
&P_r^{R_Y} \approx P_t \frac{G_t G_r \mu_x^2 \mu_y^2 A^2 N^2 M^2}{16\pi^2 d_t^3 d_r^3} \left(-x_t \sin\sigma + z_t \cos\sigma\right) \\
&\times \left(-x_r \sin\sigma + z_r \cos\sigma\right) \\
&= P_r^{\mathrm{SISO}} \frac{(-x_t \sin\sigma + z_t \cos\sigma)(-x_r \sin\sigma + z_r \cos\sigma)}{z_t z_r}, \\
&\text{and} P_r^{R_Z} \approx P_t \frac{G_t G_r \mu_x^2 \mu_y^2 A^2 N^2 M^2}{16\pi^2 d_t^3 d_r^3} z_t z_r \\
&= P_r^{\mathrm{SISO}}.
\end{aligned}
$$

Therefore, (14) is proved.

PROF OF FORMULA (18)

In the MBSU scenario, the energy received at R_x from Tx_1 consists of the reflections from the RIS elements in group E_1 and those in group E_2. Thus, the received signal power from Tx_1 can be described as:

$$
\begin{aligned}
&P_r^{Tx1} = P_t \frac{G_t G_r \mu_x \mu_y}{16\pi^2} \\
&\times \left| \begin{aligned} &\sum_{(m,n)\in E_1} \frac{\sqrt{\xi_{m,n}}}{d_t^{m,n} d_r^{m,n}} A e^{-j\left(\frac{2\pi(d_t^{m,n}+d_r^{m,n})}{\lambda} - \omega_{m,n}^{Tx1}\right)} \\ &+ \sum_{(m,n)\in E_2} \frac{\sqrt{\xi_{m,n}}}{d_t^{m,n} d_r^{m,n}} A e^{-j\left(\frac{2\pi(d_t^{m,n}+d_r^{m,n})}{\lambda} - \omega_{m,n}^{Tx2}\right)} \end{aligned} \right|^2 .
\end{aligned}
$$

Because of the far-field conditions, $d_t^{m,n} \approx d_t$ and $d_r^{m,n} \approx d_r$. Then by substituting $G = 4\pi\mu_x\mu_y/\lambda^2$ and (4) into the above equation, we obtain:

$$
\begin{aligned}
&P_r^{Tx1} \approx P_t \frac{G_t G_r \mu_x \mu_y}{16\pi^2} \\
&\times \left| \begin{aligned} &\sqrt{\frac{z_{t1}}{d_{t1}} \frac{z_r}{d_r}} \frac{A}{d_{t1} d_r} \sum_{(m,n)\in E_1} e^{-j\left(\frac{2\pi(d_{t1}^{m,n}+d_r^{m,n})}{\lambda} - \omega_{m,n}^{Tx1}\right)} \\ &+ \sqrt{\frac{z_{t1}}{d_{t1}} \frac{z_r}{d_r}} \frac{A}{d_{t1} d_r} \sum_{(m,n)\in E_2} e^{-j\left(\frac{2\pi(d_{t1}^{m,n}+d_r^{m,n})}{\lambda} - \omega_{m,n}^{Tx2}\right)} \end{aligned} \right|^2 \\
&= P_t \frac{G_t G_r \mu_x \mu_y A^2 z_r}{16\pi^2} \frac{z_{t1}}{d_{t1}^3} \\
&\times \left| \begin{aligned} &\sum_{(m,n)\in E_1} e^{-j\left(\frac{2\pi(d_{t1}^{m,n}+d_r^{m,n})}{\lambda} - \omega_{m,n}^{Tx1}\right)} \\ &+ \sum_{(m,n)\in E_2} e^{-j\left(\frac{2\pi(d_{t1}^{m,n}+d_r^{m,n})}{\lambda} - \omega_{m,n}^{Tx2}\right)} \end{aligned} \right|^2 .
\end{aligned}
$$

Similarly, we can derive the expression for the signal energy received at R_x from Tx_2 as:

$$
\begin{aligned}
&P_r^{Tx2} \approx P_t \frac{G_t G_r \mu_x \mu_y A^2 z_r}{16\pi^2} \frac{z_{t2}}{d_{t2}^3} \\
&\times \left| \begin{aligned} &\sum_{(m,n)\in E_1} e^{-j\left(\frac{2\pi(d_{t2}^{m,n}+d_r^{m,n})}{\lambda} - \omega_{m,n}^{Tx1}\right)} \\ &+ \sum_{(m,n)\in E_2} e^{-j\left(\frac{2\pi(d_{t2}^{m,n}+d_r^{m,n})}{\lambda} - \omega_{m,n}^{Tx2}\right)} \end{aligned} \right|^2 .
\end{aligned}
$$

Finally, by summing the energy expressions from Tx_1 and Tx_2, we obtain (18).

PROF OF FORMULA (25)

When the UAV moves to the optimal position U_0' (x_u, y_u, z_u), located collinear with Tx_1 and Tx_2, the received energy from Tx_1/ Tx_2 can be expressed as given by (9):

$$P_r^{T_{1/2}} \approx P_t \frac{G_t G_r \mu_x^2 \mu_y^2 A^2 (NM)^2 \left(z_{t1/2} - z_u\right)\left(z_r - z_u\right)}{16\pi^2 \left(d'_{t1/2} d'_r\right)^3}.$$

Moreover, since the RIS is equally divided into two parts, with one half assigned to Rx_1 and the other to Rx_2, Rx_1 only receives signals from Tx_1 and Tx_2 that are reflected by half of the RIS elements. Therefore, the received energy at Rx_1 can be expressed as:

$$\begin{aligned} & P_{r1}^{MIMO} \approx P_t \tfrac{G_t G_r \mu_x^2 \mu_y^2 A^2 \left(\frac{1}{2}NM\right)^2 (z_{t1}-z_u)(z_{r1}-z_u)}{16\pi^2 \left(d'_{t1} d'_{r1}\right)^3} \\ & +P_t \tfrac{G_t G_r \mu_x^2 \mu_y^2 A^2 \left(\frac{1}{2}NM\right)^2 (z_{t2}-z_u)(z_{r1}-z_u)}{16\pi^2 \left(d'_{t2} d'_{r1}\right)^3} \\ & = P_t \tfrac{G_t G_r \mu_x^2 \mu_y^2 A^2 \left(\frac{1}{2}NM\right)^2 (z_{r1}-z_u)}{16\pi^2 \left(d'_{r1}\right)^3} \left(\tfrac{(z_{t1}-z_u)}{\left(d'_{t1}\right)^3} + \tfrac{(z_{t2}-z_u)}{\left(d'_{t2}\right)^3} \right). \end{aligned}$$

Similarly, we can obtain the expression for the received energy at Rx_1 as:

$$\begin{aligned} & P_{r2}^{MIMO} \approx P_t \tfrac{G_t G_r \mu_x^2 \mu_y^2 A^2 \left(\frac{1}{2}NM\right)^2 (z_{r2}-z_u)}{16\pi^2 \left(d'_{r2}\right)^3} \\ & \times \left(\tfrac{(z_{t1}-z_u)}{\left(d'_{t1}\right)^3} + \tfrac{(z_{t2}-z_u)}{\left(d'_{t2}\right)^3} \right). \end{aligned}$$

REFERENCES

[1] M. W. Akhtar, S. A. Hassan, R. Ghaffar, H. Jung, S. Garg, and M. S. Hossain, "The shift to 6G communications: vision and requirements," Hum. Cent. Comput. Inf. Sci., vol. 10, no.1, pp. 53, Dec. 2020.

[2] C.-X. Wang et al., "On the Road to 6G: Visions, Requirements, Key Technologies, and Testbeds," IEEE Commun. Surv. Tutorials, vol. 25, no.2, pp. 905–974, 2023.

[3] W. Hong et al., "The Role of Millimeter-Wave Technologies in 5G/6G Wireless Communications," IEEE J. Microw., vol. 1, no.1, pp. 101–122, Jan. 2021.

[4] C.-X. Wang, J. Huang, H. Wang, X. Gao, X. You, and Y. Hao, "6G Wireless Channel Measurements and Models: Trends and Challenges," IEEE Veh. Technol. Mag., vol. 15, no.4, pp. 22–32, Dec. 2020.

[5] A. E. C. Redondi, C. Innamorati, S. Gallucci, S. Fiocchi, and F. Matera, "A Survey on Future Millimeter-Wave Communication Applications," IEEE Access, vol. 12, pp. 133165–133182, 2024.

[6] A. M. Al-Samman et al., "Millimeter Wave Propagation Measurements and Characteristics for 5G System," Applied Sciences, vol. 10, no.1, pp. 335, Jan. 2020.

[7] A. Al-Saman, M. Cheffena, O. Elijah, Y. A. Al-Gumaei, S. K. Abdul Rahim, and T. Al-Hadhrami, "Survey of Millimeter-Wave Propagation Measurements and Models in Indoor Environments," Electronics, vol. 10, no.14, pp. 1653, Jul. 2021.

[8] A. C. Pogaku, D.-T. Do, B. M. Lee, and N. D. Nguyen, "UAV-Assisted RIS for Future Wireless Communications: A Survey on Optimization and Performance Analysis," IEEE Access, vol. 10, pp. 16320–16336, 2022.

[9] P. Wang, J. Fang, X. Yuan, Z. Chen, and H. Li, "Intelligent Reflecting Surface-Assisted Millimeter Wave Communications: Joint Active and Passive Precoding Design," IEEE Trans. Veh. Technol., vol. 69, no.12, pp. 14960–14973, Dec. 2020.

[10] Md. A. L. Sarker, W. Son, and D. S. Han, "RIS-Assisted Hybrid Beamforming and Connected User Vehicle Localization for Millimeter Wave MIMO Systems," Sensors, vol. 23, no.7, pp. 3713, Apr. 2023.

[11] D. Zhao, G. Wang, J. Wang, and Z. Zhou, "Reconfigurable Intelligent Surface-Assisted Millimeter Wave Networks: Cell Association and Coverage Analysis," Electronics, vol. 12, no.20, pp. 4270, Oct. 2023.

[12] Y. Yang, S. Dang, M. Wen, B. Ai, and R. Qingyang Hu, "Blockage-Aware Robust Beamforming in RIS-Aided Mobile Millimeter Wave MIMO Systems," IEEE Trans. Wireless Commun., vol. 23, no.11, pp. 16906–16921, Nov. 2024.

[13] S. Hassouna et al., "A survey on reconfigurable intelligent surfaces: Wireless communication perspective," IET Commun., vol. 17, no.5, pp. 497–537, Mar. 2023.

[14] B. Shang, E. S. Bentley, and L. Liu, "UAV Swarm-Enabled Aerial Reconfigurable Intelligent Surface: Modeling, Analysis, and Optimization," IEEE Trans. Commun., vol. 71, no.6, pp. 3621–3636, Jun. 2023.

[15] E. M. Mohamed, S. Hashima, and K. Hatano, "Energy Aware Multiarmed Bandit for Millimeter Wave-Based UAV Mounted RIS Networks," IEEE Wireless Commun. Lett., vol. 11, no.6, pp. 1293–1297, Jun. 2022.

[16] C. Sriharsha and C. S. R. Murthy, "A Novel Cellular User Offloading via UAV-Borne IRS," IEEE Wireless Commun. Lett., vol. 12, no.10, pp. 1736–1740, Oct. 2023.

[17] H. Mei, K. Yang, J. Shen, and Q. Liu, "Joint Trajectory-Task-Cache Optimization With Phase-Shift Design of RIS-Assisted UAV for MEC," IEEE Wireless Commun. Lett., vol. 10, no.7, pp. 1586–1590, Jul. 2021.

[18] B. Xiong, Z. Zhang, C. Pan, and J. Wang, "Performance Analysis of Aerial RIS Auxiliary mmWave Mobile Communications With UAV Fluctuation," IEEE Wireless Commun. Lett., vol. 13, no.4, pp. 1183–1187, Apr. 2024.

[19] A. Bansal, N. Agrawal, K. Singh, C.-P. Li, and S. Mumtaz, "RIS Selection Scheme for UAV-Based Multi-RIS-Aided Multiuser Downlink Network With Imperfect and Outdated CSI," IEEE Trans. Commun., vol. 71, no.8, pp. 4650–4664, Aug. 2023.

[20] N. Agrawal, A. Bansal, K. Singh, C.-P. Li, and S. Mumtaz, "Finite Block Length Analysis of RIS-Assisted UAV-Based Multiuser IoT Communication System With Non-Linear EH," IEEE Trans. Commun., vol. 70, no.5, pp. 3542–3557, May 2022.

[21] X. Liu, Y. Yu, F. Li, and T. S. Durrani, "Throughput Maximization for RIS-UAV Relaying Communications," IEEE Trans. Intell. Transport. Syst., vol. 23, no.10, pp. 19569–19574, Oct. 2022.

[22] Y. Yu, X. Liu, and V. C. M. Leung, "Fair Downlink Communications for RIS-UAV Enabled Mobile Vehicles," IEEE Wireless Commun. Lett., vol. 11, no.5, pp.

1042–1046, May 2022.

[23] H. Zhang, M. Huang, H. Zhou, X. Wang, N. Wang, and K. Long, “Capacity Maximization in RIS-UAV Networks: A DDQN-Based Trajectory and Phase Shift Optimization Approach,” IEEE Trans. Wireless Commun., vol. 22, no.4, pp. 2583–2591, Apr. 2023.

[24] W. Wang, W. Ni, H. Tian, Y. C. Eldar, and D. Niyato, “UAV-Mounted Multi-Functional RIS for Combating Eavesdropping in Wireless Networks,” IEEE Wireless Commun. Lett., vol. 12, no.10, pp. 1667–1671, Oct. 2023.

[25] H. Yang, S. Liu, L. Xiao, Y. Zhang, Z. Xiong, and W. Zhuang, “Learning-Based Reliable and Secure Transmission for UAV-RIS-Assisted Communication Systems,” IEEE Trans. Wireless Commun., vol. 23, no.7, pp. 6954–6967, Jul. 2024.

[26] X. Tang et al., “Secure Communication With UAV-Enabled Aerial RIS: Learning Trajectory With Reflection Optimization,” IEEE Trans. Intell. Veh., pp. 1–10, 2024.

[27] S. A. H. Mohsan, M. A. Khan, M. H. Alsharif, P. Uthansakul, and A. A. A. Solyman, “Intelligent Reflecting Surfaces Assisted UAV Communications for Massive Networks: Current Trends, Challenges, and Research Directions,” Sensors, vol. 22, no.14, pp. 5278, Jul. 2022.

[28] H. Zhao et al., “Air Reconfigurable Intelligent Surface Enhanced Multiuser NOMA System,” IEEE Internet Things J., vol. 11, no.1, pp. 29–39, Jan. 2024.

[29] T. P. Truong, V. D. Tuong, N.-N. Dao, and S. Cho, “FlyReflect: Joint Flying IRS Trajectory and Phase Shift Design Using Deep Reinforcement Learning,” IEEE Internet Things J., vol. 10, no.5, pp. 4605–4620, Mar. 2023.

[30] W. Tang et al., “Wireless Communications With Reconfigurable Intelligent Surface: Path Loss Modeling and Experimental Measurement,” IEEE Trans. Wireless Commun., vol. 20, no.1, pp. 421–439, Jan. 2021.

[31] W. Tang et al., “Path Loss Modeling and Measurements for Reconfigurable Intelligent Surfaces in the Millimeter-Wave Frequency Band,” IEEE Trans. Commun., vol. 70, no.9, pp. 6259–6276, Sep. 2022.

Zhongxu Liu received the B. Eng. degree from Fuzhou University in 2018 and the M. Sc. degree from the Department of Electronic and Information Engineering, The Hong Kong Polytechnic University in 2020. He is currently pursuing the Ph.D. degree with the Department of Electrical and Electronic Engineering, The Hong Kong Polytechnic University. His research interests are focused on optical wireless communication, optical wireless positioning, and intelligent reflecting surface aided communications.

Dawei Xie received the B.Sc. degree in applied physics from Jinan University, Guangzhou, Guangdong, China, in 2021, and the M.Sc. degree in electronic and information engineering from The Hong Kong Polytechnic University, Hong Kong SAR, China, in 2024. He is currently a Research Assistant with the Photonics Research Center, The Hong Kong Polytechnic University Shenzhen Research Institute. His research interests include optical wireless communication, optical wireless positioning, and optical devices.

Luyao Wang received the B.E. in Internet of Things Engineering and B.Ec. in Finance from Jinan University, Guangzhou, Guangdong, China in 2023. Currently, she is pursuing a M.E. in Electronic and Information Engineering. Her research interests revolve around optical communication, satellite communication and resource allocation, especially in the context of satellite-ground integration.

Junbin Fang (*Member, IEEE*) is currently a full professor in the Department of Optoelectronic Engineering, Jinan University, Guangzhou, Guangdong. He received his Ph.D. degree from the South China Normal University in 2008. He was a visiting professor at the University of Toronto in Canada. His interests include visible light communication, AI security and quantum cryptography.

Zixian Wei (*Member, IEEE*) the Marconi Society’s young scholar, obtained Ph.D. at McGill University, Canada in 2024, MPhil with high honors from Tsinghua University, China in 2020, and Bachelor degree with honors from Jinan University, China in 2017, respectively. He was awarded SPIE (22’) and IEEE Photonics Society (23’) Graduate Student Awards, and PCS Tingye Li Memorial Scholarship Award (24’). His current research focuses on integrated photonics, digital signal processing, free-space/fiber optical communication, and access networks.

Changyuan Yu (*Senior Member, IEEE*) received the Ph.D. degree in electrical engineering from the University of Southern California, Los Angeles, CA, USA, in 2005. He was a visiting researcher at NEC Labs America in Princeton, USA in 2005. He then joined the faculty of National University of Singapore (NUS) in 12/2005, where he served as the founding leader of Photonic System Research Group in Department of Electrical and Computer Engineering. He was also a joint senior scientist with Institute for Infocomm Research (I2R), Agency for Science, Technology and Research (A*STAR) in Singapore. In 12/2015, he joined The Hong Kong Polytechnic University, where he is now a full professor in Department of Electronic and Information Engineering, while he also continues as an adjunct faculty member of NUS. His research focuses on photonic devices, subsystems, optical fiber communication and sensor systems, and biomedical instruments.